Supporting Information

of

From Polyanions to Infinite Chains: Chemical Bonding Evolution in AX_3 Polyhalides under Pressure

Enrico Bandiello,[a],# Álvaro Lobato,* [b],# Fernando Izquierdo,[b],# Hussien H. Osman,[a,c,d] Alfonso Muñoz, [e] Plácida Rodríguez-Hernandez,[e] and Francisco Javier Manjón*[a]

[a] Dr. E. Bandiello, Dr. H.H. Osman, Prof. Dr. F. J. Manjón
Instituto de Diseño para la Fabricación y Producción Automatizada, MALTA Consolider Team
Universitat Politècnica de València, València, Spain
Cno. De Vera, s/n, 46022 València (Spain)
E-mail: fjmanjon@fis.upv.es
[b] Dr. Á. Lobato, Dr. F. Izquierdo
Departamento de Química Física, MALTA Consolider Team
Universidad Complutense de Madrid, Madrid, Spain
Avda. Complutense, s/n, 28040 Madrid (Spain)
E-mail: alobato@ucm.es
[c] Dr. H. H. Osman
Instituto de Ciencia de los Materiales de la Universitat de València, MALTA Consolider Team
Universitat de València, Burjassot, Valencia, Spain
Cno. De Vera, s/n, 46022 València (Spain)
[d] Dr. H. H. Osman
Chemistry Department, Faculty of Science
Helwan University
Address 2, Cairo, Egypt
[e] Prof. Dr. A. Muñoz, Dr. P. Rodríguez-Hernández
Departamento de Física, Facultad de Física, MALTA Consolider Team
Universidad de La Laguna
C/. Astrofísico Francisco Sánchez, s/n, 38206 La Laguna, Tenerife (Spain)

# These authors contributed equally to this work.
*Corresponding authors

1. Experimental details

Commercial CsI_3 crystals with 99.9% purity (Sigma Aldrich) were manually ground into a fine powder using an agate mortar and pestle. Phase purity was confirmed by powder X-ray diffraction (XRD) measurements at room conditions performed with a Rigaku Ultima IV X-ray diffractometer in a parallel beam geometry. The instrument was equipped with an X-ray tube with a Cu target (Kα $\lambda = 1.5406$ Å) operated at 40 kV/40 mA and a scintillation counter detector. The diffractograms were collected keeping a constant incident angle of 5º and a scan speed of 0.3º/min. **Figure S1** shows the XRD pattern at room conditions, which evidences that the sample is a pure sample where only the orthorhombic *Pnma* phase is found. Moreover, the structural parameters obtained from LeBail fitting agree with those previously reported (see **Table S1**).

Unpolarized Raman scattering (RS) measurements excited with a 633 nm laser with a power of less than 10 mW were taken in backscattering geometry using a Horiba Jobin Yvon LabRAM HR UV microspectrometer equipped with a thermoelectrically cooled multichannel charge-coupled device detector and a 1200 grooves/mm grating, allowing a spectral resolution better than 2 cm^{-1}. The sample was loaded in a membrane-type DAC with silicon oil, and the pressure was determined via the ruby luminescence method[1], with an uncertainty of 0.1 GPa. The Raman peaks were analyzed with a Voigt profile with the Gaussian linewidth (1.6 cm^{-1}) fixed to the experimental setup resolution via FITYK software [2]. In all the experiments, DAC loading was performed while avoiding sample bridging between the diamonds.

2. Theoretical details

Ab initio total-energy calculations at 0 K for the *Pnma*, *P-3c1*, and *Pm-3n* phases of bulk CsI_3 were performed within the density functional theory (DFT)[3] framework with the Vienna Ab initio Simulation Package (VASP)[4,5]. The pseudopotential method and the projector augmented wave (PAW) scheme[6,7] were used with Cs ($5s^2$, $5p^6$, $6s^1$) and I ($5s^2$, $5p^5$) electrons treated as valence electrons and with the plane-wave basis set extended to an energy cutoff of 350 eV. The generalized gradient approximation (GGA), with the Perdew–Burke–Ernzerhof parametrization[8], and the dispersion correction DFT-D3 method of Grimme with the Becke-Johnson damping function[9] were used to describe the exchange and correlation energy. The Brillouin zones of these structures were sampled with dense Monkhorst–Pack meshes[10] of special *k*-points: 4 × 6 × 4 for the orthorhombic *Pnma* (*Pbnm* or *Pmcn*, space group No. 62) phase, 6 × 6 × 4 for the hexagonal *P*-3*c*1 (space group No. 165) phase, and 6 × 6 × 6 for the cubic *Pm*-3*n* (space group No. 223) phase. With this method, a high convergence of 1–2 meV per formula unit in the total energy and an accurate calculation of the forces on atoms are obtained. For each of the studied phases, the structures were fully relaxed to the optimized configuration, at sets of selected volumes through the calculation of the forces on atoms and the stress tensor. Two optimization criteria were used: (i) forces on the atoms should be lower than 0.004 eV/Å, and (ii) deviations of the stress tensor from the diagonal hydrostatic form should be lower than 0.1 GPa. We have used a direct force constant approach [11] to obtain the lattice-dynamical properties, wavenumber, and symmetry of the phonon modes at the Γ point of the Brillouin zone for the different phases.

A density-based approach grounded in the Quantum Theory of Atoms in Molecules (QTAIM) was employed to analyze the electron density topology of CsI_3. Quantum ESPRESSO (version 6.5)[12] was utilized for this analysis, in conjunction with wannier90[13] and the CRITIC2 programs.[14] Single-point calculations were performed at the VASP equilibrium geometries, using the same uniform *k*-point grids mentioned above. A plane-wave cutoff of 100 Ry and a density cutoff of 400 Ry were consistently applied. Norm-conserving pseudopotentials for the Kohn-Sham states and PAW data sets for the all-electron density were sourced from the pslibrary.[15] Delocalization index (DI) calculations, used to determine the number of electrons shared (ES) as 2×DI, were conducted using a Wannier transformation as described in Ref.[16]

On the other hand, an orbital-based method has also been used to analyze the multicenter character of the different I−I bonds in the different phases of CsI_3 by calculating the ICOBI(2c) and ICOBI(3c) parameters which stands for the integrated Crystal Orbital Bond Index as detailed in Ref. [17]. For this purpose, the *Local Orbital Basis Suite Towards Electronic-Structure Reconstruction* (LOBSTER) package was used.[18] In addition, other parameters such as projected Crystal Orbital Hamiltonian Population (pCOHP) and its integrated value (ICOHP) for different bonds have been calculated with this software.

3. Structural properties

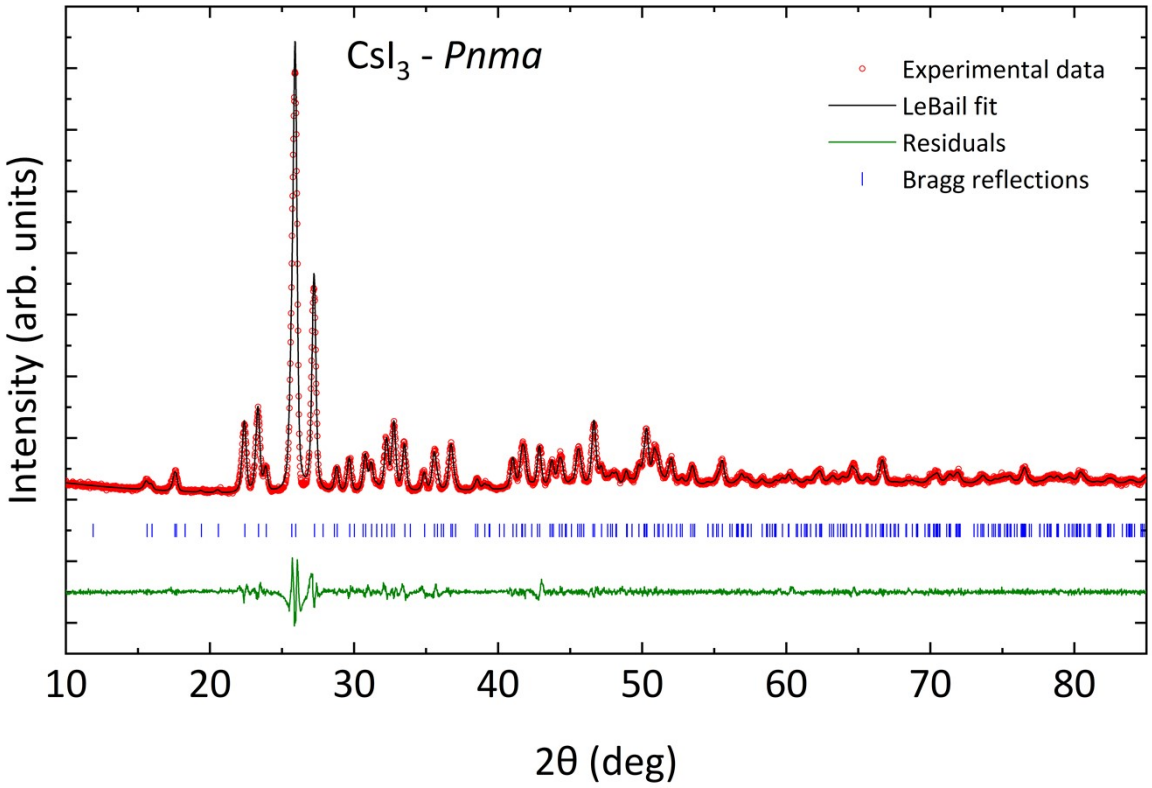

Figure S1. XRD pattern and LeBail fit of powder CsI_3 at room pressure in the *Pnma* phase, as obtained with a Rigaku diffractometer using filtered Cu K_α radiation. Red circles: experimental data; black line: LeBail fit; blue ticks: Bragg reflections; green line: residuals. The cell parameters as obtained by the fit, are a=11.0804(4) Å, b=6.85977(25) Å, c=10.0260(4) Å and Vol=762.1(3) Å^3, in good agreement with those obtained by Patel *et al.* (Ref. [19]).

Table S1. Structural parameters of the experimental *Pnma*, *P*-3*c*1, and *Pm*-3*n* phases at 0 GPa, 12.2 GPa, and 26.8 GPa[19], respectively, and simulated at 0 GPa, 1.8 GPa, and 22.6 GPa, respectively.

	Pnma			***P*-3*c*1**		***Pm*-3*n***	
	Exp.[a]	*Exp.*[b]	*The.*[a]	*Exp.*[b]	*The.*[a]	*Exp.*[b]	*The.*[a]
a (Å)	11.0804(4)	11.084	10.901	8.790	8.792	5.905	5.915
b(Å)	6.85977(25)	6.844	6.836				
c (Å)	10.0260(4)	10.026	10.142	10.878	10.820		
Vol (Å^3)	762.1(3)	761	756	727.8	724.3	206	207

[a] This work
[b] From Ref. [19]

Table S2. Theoretical values of the short and long I–I bonds in the *Pnma*, *P*-3*c*1, and *Pm*-3*n* phases at selected pressures. Note that in the *Pnma* phase, the short and long bonds are intramolecular bonds of the I_3^- unit, whereas in the *P*-3*c*1 phase, the short and long bonds correspond to intramolecular (within I_3^- units) and intermolecular (between I_3^- units) bonds. In the *Pm*-3*n* phase, there is only a single I–I bond.

Bond	**Phase**					
	Pnma (0 GPa)		*P*-3*c*1 (2.08 - 1.8 GPa)		*Pm*-3*n* (26.8 - 27.3 GPa)	
	Exp.[a]	*The.*[b]	*Exp.*[a]	*The.*[b]	*Exp.*[a]	*The.*[b]
$I_{(1)}$-$I_{(2)}$ (Å)	2.839	2.896	-	-	-	-
$I_{(1)}$-$I_{(3)}$ (Å)	3.041	3.023	-	-	-	-
I-I (intra) (Å)	-	-	2.945	2.948	-	-
I-I (inter) (Å)	-	-	4.241	4.295	-	-
I-I (Å)	-	-	-	-	2.952	2.919

[a] From Ref. [19]
[b] This work

Table S3: Comparison between experimental and calculated (in parentheses) atomic positions for the *Pnma*, *P-3c1* and *Pm-3n* three different phases of CsI_3 at selected pressures, similar to those reported in Ref. [19].

Phase	**Pressure** (GPa) Experiment[a] (*calculation*)[b]	**Atom**	**Wyckoff position**	**Atomic coordinates** Experimental[a] (*calculated*)[b]		
Orthorhombic (*Pnma*)	0.9 (*0.9*)	Cs1	4*c*	0.8320 (*0.81576*)	0.2500 (*0.25000*)	0.0348 (*0.47101*)
		I1	4*c*	0.5732 (*0.55904*)	0.2500 (*0.25000*)	0.7393 (*0.73656*)
		I2	4*c*	0.3804 (*0.3668*)	0.2500 (*0.25000*)	0.5455 (*0.55726*)
		I3	4c	0.1636 (*0.16657*)	0.2500 (*0.25000*)	0.3535 (*0.37123*)
Trigonal (*P-3c1*)	12.2 (*11.6*)	Cs1	2*b*	0.0000 (*0.00000*)	0.0000 (*0.00000*)	0.0000 (*0.00000*)
		Cs2	4*d*	0.3333 (*0.33333*)	0.6666 (*0.66667*)	0.8304 (*0.84355*)
		I1	6*f*	0.2405 (*0.25319*)	0.0000 (*0.0000*)	0.2500 (*0.25000*)
		I2	12*g*	0.3488 (*0.31816*)	0.4294 (*0.41144*)	0.0699 (*0.09197*)
Cubic (*Pm-3n*)	26.8 (27.3)	Cs	2*a*	0.0000 (*0.00000*)	0.0000 (*0.00000*)	0.0000 (*0.00000*)
		I	6*c*	0.2500 (*0.25000*)	0.000 (*0.00000*)	0.5000 (*0.50000*)

[a] From Ref. [19]
[b] This work

Table S4. Experimental[19,20] and theoretical values of the volume, bulk modulus, and its pressure derivative at room pressure, according to Vinet[21] and third-order Birch–Murnaghan (BM3)[22] equations of state (EOS), for the *Pnma*, *P*-3*c*1, and *Pm*-3*n* phases of CsI_3.

	Pnma			***P-3c1***			***Pm-3n***	
	Exp.	BM3	Vinet	Exp.	BM3	Vinet	BM3	Vinet
V_0 (Å^3)	766.4(16)[a]	755.90	–	1034(6)	1089.92	1093.28	306.99	312.14
B_0 (GPa)	5.6(6)[a] 5(1)[b]	8.57	–	17.7(9)[a] 17.9(8)[b]	8.00	6.85	22.70	19.17
$B_0^{'}$	12(2)[a] 13(4)[b]	5.59	–	3.94(12)[a] 4[b]	5.81	6.79	4.67	5.44

[a] From Ref. [19]
[b] From Ref. [20]

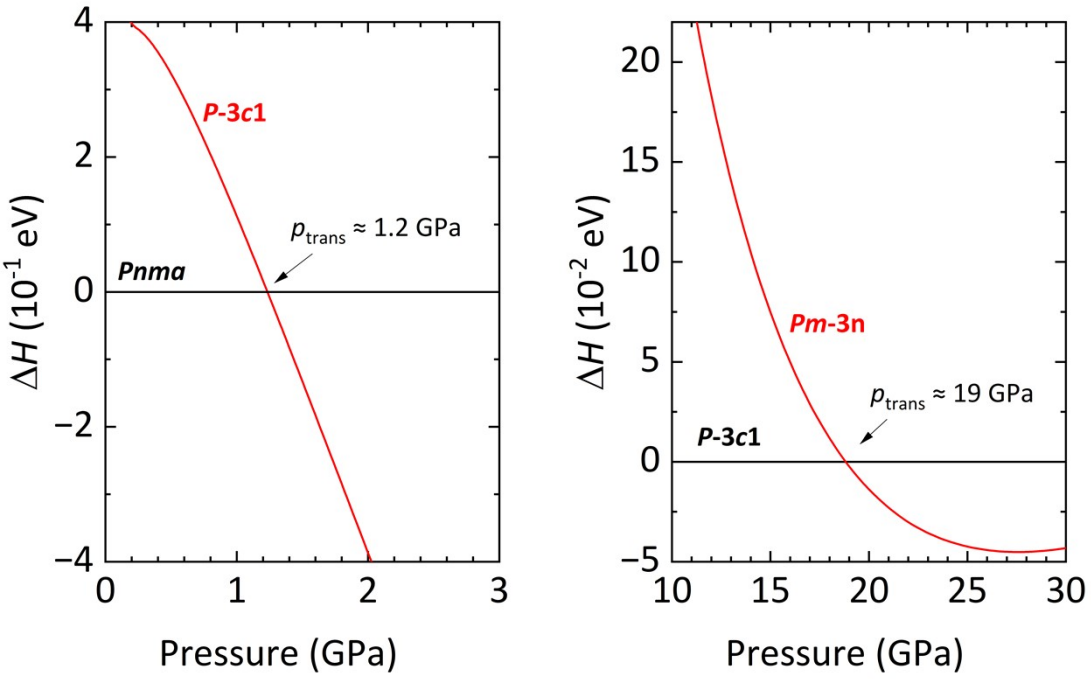

Figure S2. Enthalpy difference ΔH vs. pressure between the *Pnma* and *P*-3*c*1 phases (left) and between the *Pm*-3*n* and *P*-3*c*1 phases (right) in the pressure region of interest. The enthalpy of the *Pnma* and *P*-3*c*1 phases was taken as reference (balck line with 0 value) in each figure, respectively.

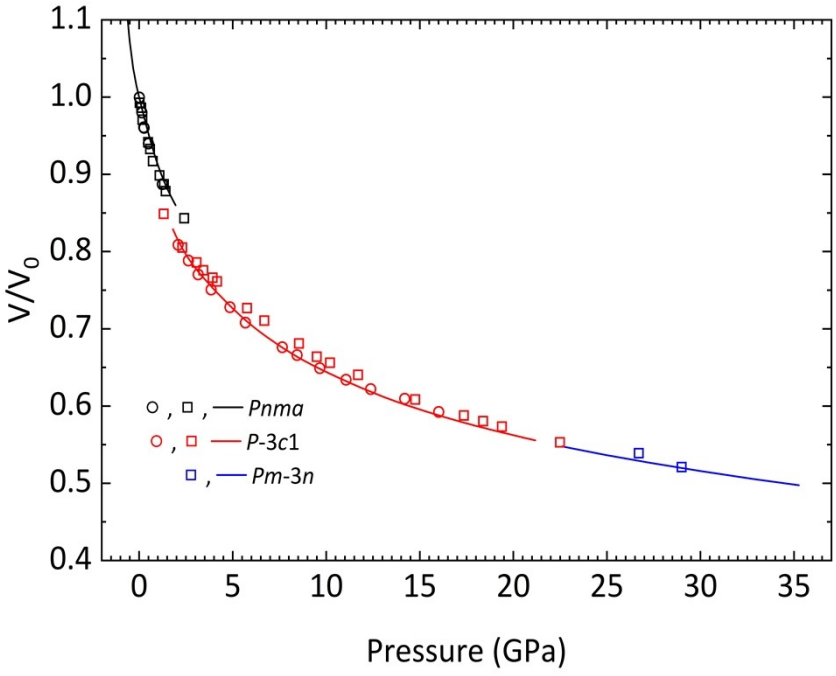

Figure S3. Experimental (symbols) and theoretical (lines) pressure dependence of the normalized unit-cell volume per formula unit. Open squares correspond to Ref. [19], and open circles correspond to Ref. [20].

Figure S3 confirms that the *Pnma*-to-*P*-3*c*1 phase transition is surely a weak first-order phase transition, and so is likely the *P*-3*c*1-to-*Pm*-3*n* transition, since no direct group-subgroup relationship is present between these structures. Notice that there is no apparent discontinuity in the equation of state (EOS) for the *P*-3*c*1-to-*Pm*-3*n* phase transition, which thus has almost a second-order character. In fact, some of the atomic parameters of the *P*-3*c*1 phase tend to high-symmetry values as pressure increases (**Figure S4**), as expected for a phase transition from a hexagonal structure to a cubic structure.

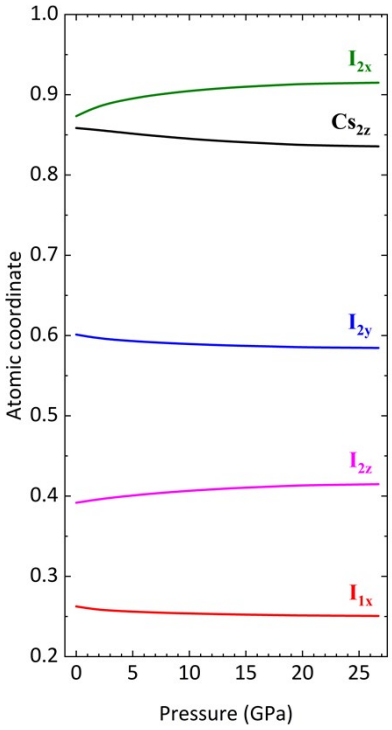

Figure S4. Pressure dependence of the non-fixed atomic coordinates of the Cs_2, I_1, and I_2 atoms in the *P*-3*c*1 phase of CsI_3. The atomic positions of the Cs_1, Cs_2, I_1, and I_2 atoms are (0, 0, 0), (1/3, 2/3, Cs_{2z}), (I_{1x}, 0, 1/4) and (I_{2x}, I_{2y}, I_{2z}), respectively. Note how the I_{1x} atomic coordinate tends to the value ¼, thus tending toward a more symmetric structure such as the *Pm*-3*n* phase.

3.1. Discussion on the total bond length of the I_3^- polyanion from Figure 2a.

The *Pnma* phase has two I−I bond distances corresponding to the two distances within the asymmetric I_3^- polyanion. Both distances exhibit an expected decrease with increasing pressure (see **Figure 2a** in the main text). This is consistent with the decrease of experimental total length of the I_3^- polyanion from 5.88 Å at room pressure (RP) to 5.86 Å at 1.25 GPa.[20] The extrapolation of these experimental results to higher pressures yields that the total length of the I_3^- polyanion decreases below 5.8 Å above ca. 7 GPa. This value is in agreement with the already discussed range of stability of the asymmetric I_3^- polyanion units.[23,24] Above ca. 1 GPa, the *P*-3*c*1 exhibits symmetric I_3^- polyanions. However, it has been reported that both *Pnma* and *P*-3*c*1 phases coexist up to 6 to 10 GPa;[19] a result justified by the range of stability of the asymmetric I_3^- polyanions mentioned above (up to 7 GPa).[23,24] The experimental total distance length of the I_3^- anion is 2 × 2.945 Å = 5.89 Å at ca. 2.0 GPa,[20] a value in notable agreement with our calculations. It is important to note here that pressure is a thermodynamic variable which helps in the symmetrization of the I_3^- polyanions, as was already suggested,[25] thus favoring the formation of multicenter bonds, as recently proposed.[26–28]

3.2. Discussion on the three stages of multicenter bond formation in CsI_3 from Figure 2a.

The recent unified theory of multicenter bonding (i.e., involving more than two atoms) proposes that the formation of a multicenter bond between atoms A, B, and C, hereafter noted as A−B−C, takes place from an original short primary iono-covalent bond (A−B with bond length d_1) and a long secondary non-covalent interaction (a nascent B···C bond, with bond length d_2), proceeding via a three-stage process.[27,28]

Stage 1 features a short primary bond and a long secondary bond that are so different in length (typically $d_2/d_1 > 2$) that *no interaction* is present between them. In this stage, both bond primary and secondary bond lengths show a normal decrease as pressure increases. Stage 2 occurs when both the primary and the incipient bonds are relatively close in length (typically $1 < d_2/d_1 < 2$). In this stage, an actual interaction is present (*trans influence*), which leads to an equalization of both bond lengths in such a way that the primary bond length increases with pressure, the secondary bond length shows a normal decrease with increasing pressure. Finally, stage 3 occurs when the primary and secondary bonds are equal or comparable in length ($d_2/d_1 \approx 1$). At this stage, it is not possible to distinguish between the primary and secondary bonds, as they both form part of a three-centers bond (A-B-C). Each one of two-center bonds constituting the three-center bond (A−B and B−C) now shows a normal decrease with increasing pressure.

These stages can be identified in CsI_3 under compression by a close inspection of **Figure 2a**. In the *Pnma* phase two I−I bond distances are present within the asymmetric I_3^- polyanion, which exhibit a normal decrease with increasing pressure. This is consistent with stage 3, in which asymmetric ERMBs are present and there is no *trans influence* of one bond over the other since both are very similar. On the contrary, the *P*-3*c*1 phase exhibits two I−I bond distances that tend to equalize. While the secondary long I−I bond distance decreases at all pressures, the short primary one within the symmetric I_3^- polyanion exhibits different stages, if we attend to experimental data.[20] Between 0 and 6 GPa, there is a normal decrease of both the intramolecular (primary) and intermolecular (secondary) I−I bonds distance with pressure, as corresponds to stage 1 in the formation of multicenter bonds. However, between 6 and 17 GPa (maximum pressure reported in

Ref. [20]), there is an anomalous increase of the intramolecular I−I bond distance with pressure. This anomalous increase of the short primary bond length is consistent with the expected stage 2 of the process of formation of multicenter bonds, which culminates with the formation of multicenter bonds in stage 3, at the onset of the *Pm*-3*n* phase. It must be noted that theoretical data show only a negligible change of the intramolecular I−I bond secondary distance on increasing pressure (unlike what happens in the *Pnma* phase), thus suggesting that only stage 2 (previous to the formation of EDMBs) occurs in the *P*-3*c*1 phase of CsI_3. In any case, it is clear that independently on the number of stages in the *P*-3*c*1 phase of CsI_3, multicenter bonds are formed at the onset of *Pm*-3*n* phase as a consequence of the *trans influence* between the two I−I bonds of the *P*-3*c*1 phase and its trend to equalization at HP. Finally, the normal pressure-driven decrease of the I−I bond distance (within the infinite linear iodine chain) in the *Pm*-3*n* phase is consistent with stage 3, in which multicenter bonds are formed. In summary, the process of equalization of the experimental and theoretical I−I bond lengths in the *P*-3*c*1 phase that culminates in the equalization of intramolecular and intermolecular I−I bond distances evidences the multicenter character of the I−I bonds of the *Pm*-3*n* phase. In principle it is not possible to say which kind of multicenter bonds (whether if ERMBs or EDMBs) are formed in the *Pm*-3*n* phase. It can be note, however, that the large bond length of the I−I bond in the *Pm*-3*n* phase (well above 2.95 Å at 22 GPa), compared to the covalent I−I bond in the I_2 molecule in solid iodine (2.74 Å at RP),[23,24] also points towards the multicenter character of the I−I bond in the *Pm*-3*n* phase. Moreover, the I−I bonds are larger in the *Pm*-3*n* phase in the intramolecular I−I bonds in the *P*-3*c*1 phase, suggesting the formation of EDMBs in the former, according to the Pauling's formula for bond order.[31]

3.3. Discussion about electron-deficient multicenter (2c-1e) bonds in infinite linear atomic chains.

As regards the bonding in the infinite linear iodine chains in the *Pm*-3*n* phase of CsI_3, it must be stressed that P−P bonds in infinite linear P^{2-} chains in a HP phase of Mo_2P[29] and Se−Se bonds in infinite linear Se^- chains in a HP phase of YSe_3[30] have been classified as electron deficient two-center one-electron bonds (2c-1*e*). Notice that both P^{2-} and Se^- atoms are pseudo-Cl and pseudo-Br atoms. These P−P and Se−Se bonds are longer than the corresponding bond distances in covalent bonds at similar pressures, thus pointing to the multicenter character of the bonds in the infinite linear atomic chains, according to the Pauling's formula for bond order.[31] In this context, it is important to stress that the experimental I−I bond distance of the *Pm*-3*n* phase at 26.8 GPa (2.9523 Å)[19] is longer than the short primary I−I bond distance of the *P*-3*c*1 phase at 2 GPa (2.945 Å)[20]. Moreover, the I−I bond distance of the *Pm*-3*n* phase is much longer than the I−I bond distance of the shorter primary bond of the electron-rich multicenter bond (ERMB) in the *Pnma* phase (2.8393 Å)[20] and also than the covalent I−I bond in the I_2 molecule in solid iodine (2.74 Å) at RP. [23,24]

The reason for the longer bond distance in the cubic *Pm*-3*n* phase of CsI_3 is that these bonds are multicentric in character, since they result from the equalization of the long secondary intermolecular I−I bond and the short primary intramolecular I−I bond due to the interaction (*trans influence*) between both bonds. This interaction leads to the increase of the short intramolecular bond. Note that in both *Pnma* and *P*-3*c*1 phases there are two types of I atoms, with one- and two-fold coordination, while in the *Pm*-3*n* phase there is only one type of I atoms with two-fold coordination. Therefore, the presence of I atoms with a coordination higher than one evidences the presence of hypercoordinated, but not

hypervalent I atoms, since neither the I atoms in the I_3^- polyanions nor the I atoms in the infinite linear iodine chains violate the octet rule, [28] unlike previously assumed.[32]

As an aside to the previous paragraph, we must comment that the extrapolation of our theoretical data for the *Pm*-3*n* phase at 0 GPa allows us to predict that the bond length expected for the 2c-1e electron-deficient multicenter bond (EDMB) in the infinite linear iodine chain at RP is of the order of 3.399 Å. We think this value is going to be important to identify EDMBs between I atoms in infinite quasi-linear iodine chains present in iodides at RP, e.g., in the pyrroloperylene-iodine complex with average I−I bond distances of the order of 3.112 Å[33]. Note that these iodine complexes show brittle behavior, as expected for materials with multicenter bonds since both EDMBs and ERMBs are directional bonds like iono-covalent bonds and unlike metallic bonds. [27,28] Also note also that the values of the I−I bond distance in the pyrroloperylene-iodine complex (experimental)[33] and in the *Pm*-3*n* phase of CsI_3 at RP (theoretical), which are both between 3.0 and 3.4 Å, and are considerably larger than the I−I bonds in covalent bonds (I_2) and ERMBs at or near RP, as discussed in the previous paragraph. This is fully consistent with the expected values for EDMBs at RP according to the recently discussed Pauling's formula for bond order in I atoms.[31]

Following the above argument, it must be mentioned that a study of the *trans influence* of intermolecular bonds in intramolecular bonds was performed in linear chains of I_2 molecules inside nanotubes as a function of temperature.[34] It has been shown that the short primary covalent I−I bond distance in the I_2 molecule increases in length as I_2 molecules become closer to each other along a given direction i.e., as the long secondary non-covalent $I_2\cdots I_2$ bond length decreases. According to simulations, an infinite linear I_2 chain, $(I_2)_\infty$, results in an intramolecular I−I bond distance length of 2.7017 Å and an intermolecular I−I bond length of 3.3695 Å (see Figure 3a in Ref. [34]), with an average bond distance of 3.0356 Å. Again, this value is longer than the value for the ERMB in the *Pnma* and *P*-3*c*1 phases of CsI_3 at or near RP, thus, supporting the formation of EDMBs in the infinite linear iodine chain (I_∞).

4. Vibrational properties

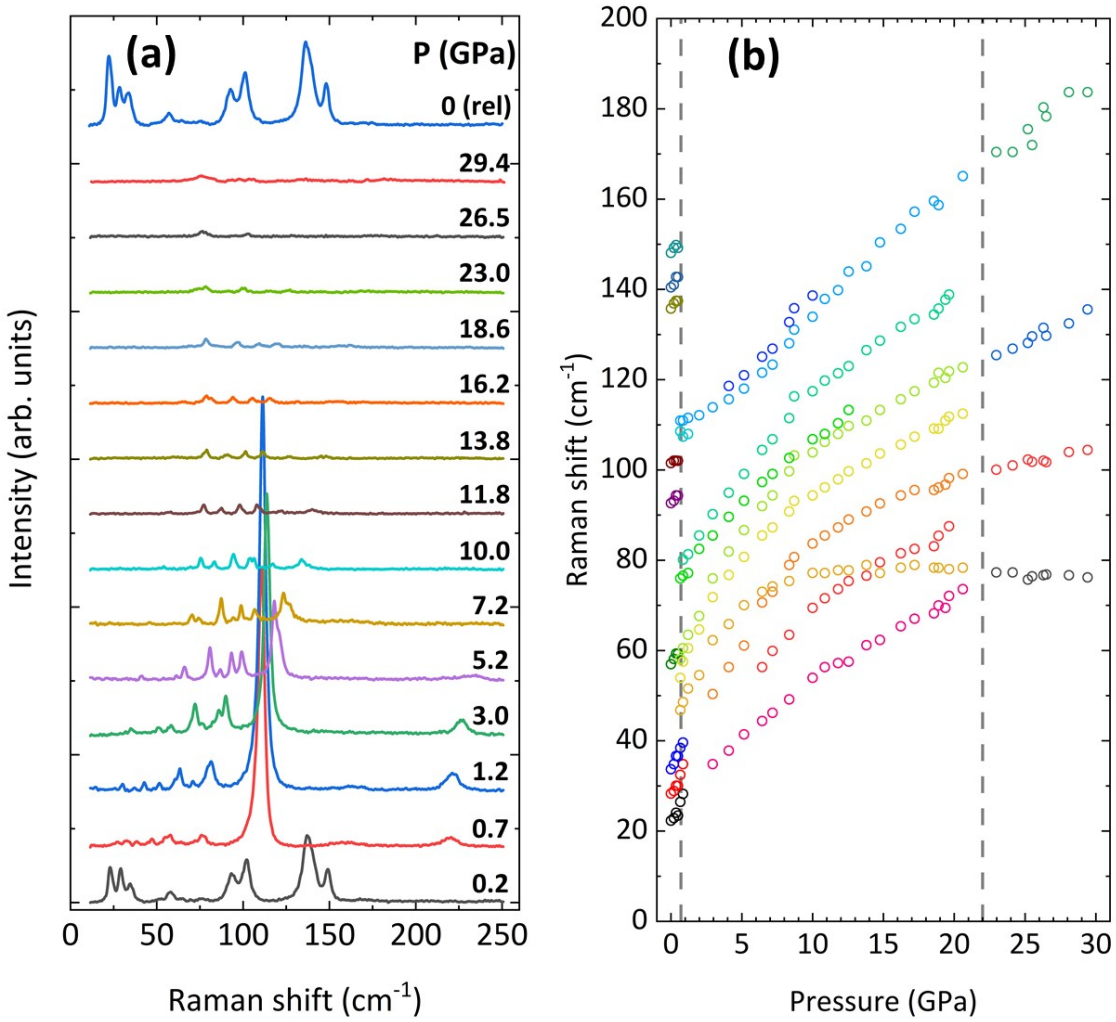

Figure S5. (a) Selection of Raman spectra of CsI_3 measured at different pressures up to 29.4 GPa; (rel) indicates the spectrum obtained at pressure release. (b) Pressure dependence of the experimental wavenumbers up to 29.4 GPa.

4.1. *Pnma* phase

According to group theory [35], the *Pnma* phase (S.G. No. 62) of CsI_3 (with four atoms in the *4c* Wyckoff sites) has 48 vibrational modes (45 optical and 3 acoustic). The mechanical representation at the Brillouin zone center (Γ point) is as follows:

Γ_{48}: $8A_g(R) + 4A_u(S) + 4B_{1g}(R) + 7B_{1u}(IR) + 8B_{2g}(R) + 3B_{2u}(IR) + 4B_{3g}(R) + 7B_{3u}(IR) + B_{1u}(ac) + B_{2u}(ac) + B_{3u}(ac)$

where R and IR stand for Raman- and infrared-active, respectively; S stands for silent; and ac stands for acoustic.

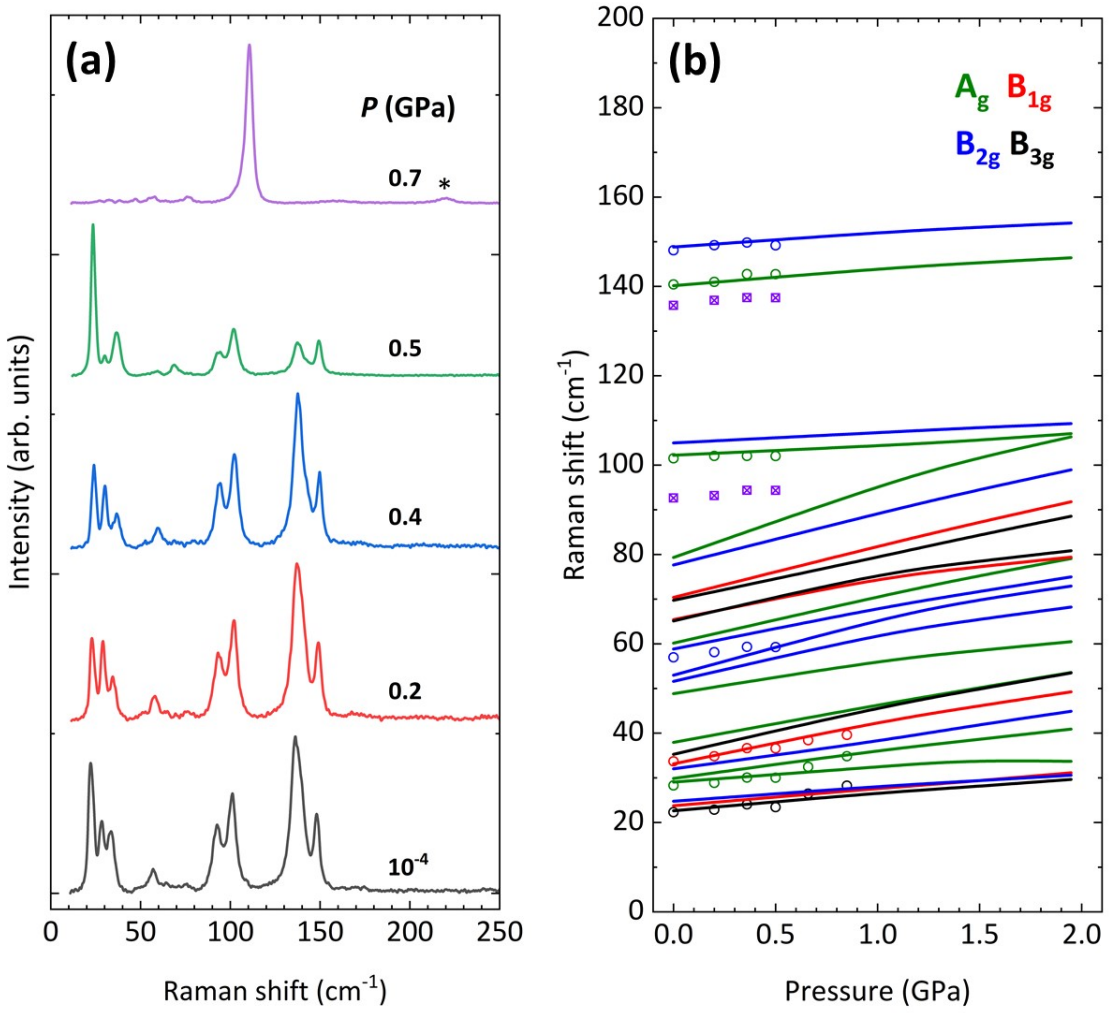

Figure S6. *Pnma* phase. (a) Selection of Raman spectra at different pressures, up to 2.0 GPa. A phase transition is already observed at 0.7 GPa to the *P*-3*c*1 phase. The asterisk indicates a band likely corresponding to an overtone of the intense mode of the *P*-3*c*1 phase at ca. 110 cm^{-1}. (b) Pressure dependence of the experimental (symbols) and theoretical (lines) Raman-active wavenumbers of the *Pnma* phase. The crossed squares in (b) indicate overtones.

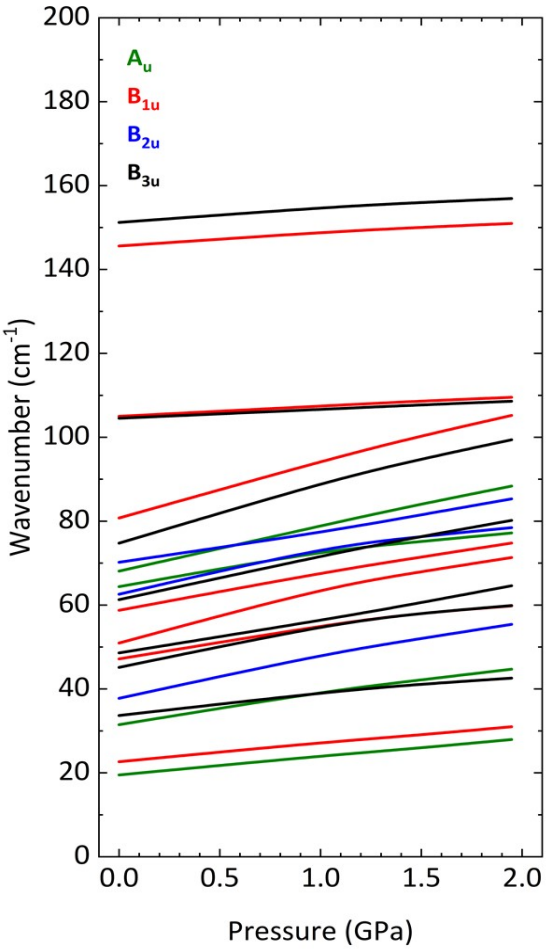

Figure S7. *Pnma* phase. Pressure dependence of the theoretical infrared (IR)-active wavenumbers.

All the high-wavenumber modes of the *Pnma* phase of CsI_3 come from the I_3^- units. In particular, the modes at 100-110 cm^{-1} and at 140-150 cm^{-1} come from the symmetrical (ν_1) and antisymmetrical (ν_3) stretching modes of the asymmetric I_3^- units, respectively [36]. Note that in isolated asymmetric I_3^- units, both ν_1 and ν_3 modes are observed in the Raman spectrum, while in isolated symmetric I_3^- units only the ν_1 mode is observed in the Raman spectrum.[36] The observation of experimental Raman modes in the region of 140-150 cm^{-1} in the *Pnma* phase of CsI_3 is consistent with the asymmetric I_3^- units in this phase.

Table S5. Experimental and theoretical wavenumbers and pressure coefficients of the Raman-active modes of the *Pnma* phase with tentative symmetry assignment of experimentally measured Raman bands. The colors correspond to those in the legend of **Figure S6b**. The experimental data were fitted linearly, because of the short experimental range.

	Fits				
	$\omega_0 + aP + bP^2$			$\omega_0 + aP$	
Assignment	**Calculations**			**Experiment**	
	ω_0 (cm^{-1})	a (cm^{-1}/GPa)	b (cm^{-1}/GPa^2)	ω_0 (cm^{-1})	a (cm^{-1}/GPa)
B_{3g}^1	22.63(15)	4.2(3)	-0.34(18)	21.6(7)	6.9(1.4)
B_{1g}^1	23.76(11)	3.85(25)	-0.04(13)		
B_{2g}^1	24.76(8)	3.60(20)	-0.31(10)		
A_g^1	29.0(5)	5.0(1.2)	-1.3(6)		
A_g^2	29.86(12)	6.76(28)	-0.57(14)	27.5(7)	7.5(1.3)
B_{2g}^2	32.00(27)	5.9(6)	0.3(3)		
B_{1g}^2	33.13(12)	10.38(29)	-1.09(15)	33.62(29)	7.0(6)
B_{3g}^2	35.27(12)	11.53(29)	-1.13(15)		
A_g^3	37.93(5)	8.72(11)	-0.35(5)		
A_g^4	48.85(15)	8.6(3)	-1.36(18)		
B_{2g}^3	51.62(17)	12.3(4)	-1.96(20)		
B_{2g}^4	52.96(9)	14.91(20)	-2.39(10)	57.1(3)	5.0(1.0)
B_{2g}^5	58.85(14)	9.9(3)	-0.86(16)		
A_g^5	60.14(6)	11.23(13)	-0.77(7)		
B_{3g}^3	65.1(4)	12.8(9)	-2.5(4)		
B_{1g}^3	65.4(3)	11.2(7)	-2.1(4)		
B_{3g}^4	69.73(13)	9.7(3)	-0.04(16)		
B_{1g}^4	70.37(7)	11.92(16)	-0.47(8)		
B_{2g}^6	77.64(10)	12.23(21)	-0.66(11)		
A_g^6	79.31(14)	18.5(3)	-2.38(16)		
A_g^7	102.21(10)	1.64(26)	0.42(12)	101.64(18)	1.0(5)
B_{2g}^7	104.97(6)	2.46(14)	-0.12(7)		
A_g^8	140.16(4)	4.33(9)	-0.58281	140.3(4)	5.2(1.3)

B_{2g}^{8}	148.803(26)	3.78(6)	-0.53(3)	148.4(5)	2.5(1.5)

Table S6. Theoretical wavenumbers and pressure coefficients of the IR-active modes of the *Pnma* phase. The colors correspond to those in the legend of **Figure S7**.

Assignment	**Fits $\omega_0 + aP + bP^2$ Calculations**		
	ω_0 (cm^{-1})	a (cm^{-1}/GPa)	b (cm^{-1}/GPa^2)
A_u^1	19.49(15)	4.6(3)	-0.13(18)
B_{1u}^1	22.67(19)	4.7(4)	-0.22(22)
A_u^2	31.50(15)	8.7(3)	-0.98(17)
B_{3u}^1	33.65(6)	6.39(14)	-0.93(7)
B_{2u}^1	37.77(17)	11.6(4)	-1.30(20)
B_{3u}^2	45.13(5)	12.35(12)	-2.45(6)
B_{1u}^2	47.14(24)	9.6(5)	-1.60(28)
B_{3u}^3	48.601(14)	7.21(3)	0.516(16)
B_{1u}^3	50.96(29)	15.2(7)	-2.5(3)
B_{1u}^4	58.75(8)	9.51(19)	-0.66(10)
B_{3u}^4	61.27(6)	11.18(14)	-0.75(7)
B_{2u}^2	62.6(3)	13.6(7)	-2.8(4)
A_u^3	64.4(3)	10.1(7)	-1.8(4)
A_u^4	68.07(11)	11.34(24)	-0.47(12)
B_{2u}^3	70.17(13)	6.54(29)	0.64(15)
B_{3u}^5	74.751(6)	16.016(14)	-1.727(7)
B_{1u}^5	80.75(9)	14.59(21)	-1.04(11)
B_{3u}^6	104.53(4)	2.17(10)	-0.05(5)
B_{1u}^6	105.00(5)	2.60(11)	-0.13(6)
B_{1u}^7	145.600(6)	3.732(15)	-0.501(7)
B_{3u}^7	151.204(17)	4.16(4)	-0.633(19)

4.2. *P*-3*c*1 phase

According to group theory,[35] the *P*-3*c*1 phase (S.G. No. 165) of CsI_3 (with four independent atoms in the *2b*, *4d*, *6f*, and *12g* Wyckoff sites) has 74 vibrational modes (71 optical and 3 acoustic). The mechanical representation at the Brillouin zone center (Γ point) is as follows:

Γ_{74}: $5A_{1g}(R) + 6A_{1u}(S) + 6A_{2g}(S) + 6A_{2u}(IR) + 11E_g(R) + 13E_u(IR) + A_{2u}(ac) + E_u(ac)$

where R and IR stand for Raman- and infrared-active, respectively; S stands for silent; and ac stands for acoustic.

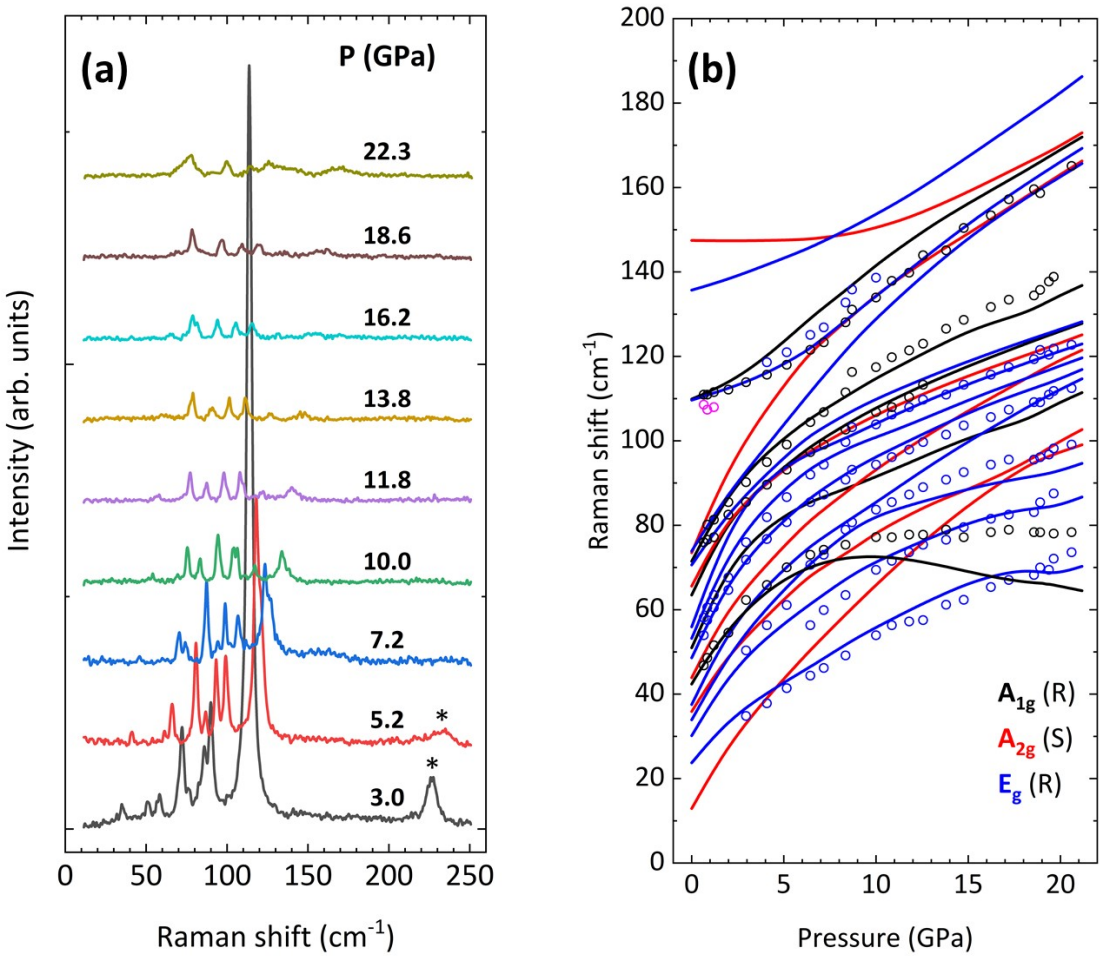

Figure S8. *P*-3*c*1 phase. (a) Selection of Raman spectra at different pressures. Asterisks indicate a band likely corresponding to an overtone of the intense mode of the *P*-3*c*1 phase at ca. 110 cm^{-1}. The Raman spectrum at 22.3 GPa, already corresponds to the *Pm*-3*n* phase. (b) Pressure dependence of the experimental (symbols) and theoretical (lines) Raman-active wavenumbers. The symbols in magenta correspond to phonons that cannot be correlated with those obtained via theoretical calculations (see **Table S7**). The dashed lines indicate silent A_{2g} phonons.

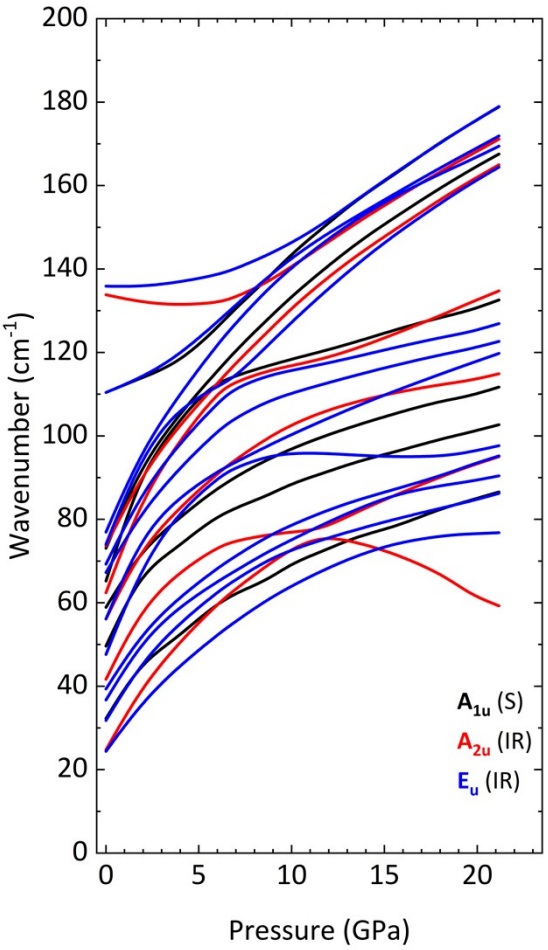

Figure S9. *P*-3*c*1 phase. Pressure dependence of the theoretical IR-active wavenumbers.

All the high-wavenumber modes of the *P*-3*c*1 phase of CsI_3 come from the I_3^- units. In particular, the modes at 100-110 cm^{-1} and 140-150 cm^{-1} come from the symmetrical and antisymmetrical stretching modes of the symmetric I_3^- units, respectively.[36] Experimentally, the symmetrical stretching modes are the only ones observed in the Raman spectrum in the isolated symmetric I_3^- units because the antisymmetrical stretching modes are only IR-active.[36] This agrees with the disappearance of the experimental modes of the region of 140-150 cm^{-1} in the *P*-3*c*1 phase of CsI_3 with only symmetric I_3^- units, unlike the *Pnma* phase that has asymmetric I_3^- units.

Table S7. Experimental and theoretical wavenumbers and pressure coefficients of the Raman-active modes ($^{A_{1g}}$, ^{E_g}) and g-type silent modes ($^{A_{2g}}$) of the P-3c1 phase, with tentative symmetry assignment of experimentally measured Raman bands. The colors correspond to those in the legend of **Figure S8b**.

Assignment	**Calculations**			**Fits** $\omega_0 + aP + bP^2$			**Experiment**		
	ω_0 (cm^{-1})	a (cm^{-1}/GPa)	b (cm^{-1}/Gpa^2)	ω_0 (cm^{-1})	a (cm^{-1}/GPa)	b (cm^{-1}/GPa^2)	ω_0 (cm^{-1})	a (cm^{-1}/GPa)	b (cm^{-1}/GPa^2)
A_{2g}^1	14.4(6)	6.27(14)	-0.106(6)						
E_g^1	24.6(7)	4.07(15)	-0.091(7)	26.1(9)	3.15(16)	-0.044(7)			
E_g^2	33.0(1.1)	5.11(23)	-0.126(10)	27.5(2.1)	5.4(4)	-0.126(14)			
E_g^3	36.8(1.5)	6.1(3)	-0.168(14)	32.8(1.7)	6.8(3)	-0.178(13)			
A_{2g}^2	39.0(1.4)	4.8(3)	-0.091(13)						
E_g^4	42.2(1.7)	5.4(4)	-0.098(17)	33.58(27)	4.2(4)	-0.078(14)			
A_{2g}^3	47.5(1.3)	5.68(29)	-0.107(12)						
A_{1g}^1	48.2(6)	4.04(14)	-0.165(6)	47.2(1.3)	4.6(3)	-0.156(15)			
E_g^5	53.6(1.9)	5.6(4)	-0.131(18)						
A_{1g}^2	58.0(2.7)	4.5(6)	-0.10(25)						
E_g^6	60.0(2.7)	5.6(6)	-0.138(26)	54.7(1.0)	5.30(24)	-0.127(11)			
E_g^7	64(3)	5.5(7)	-0.14(3)	56.7(1.4)	6.30(24)	-0.157(11)			
A_{1g}^3	68.6(1.8)	5.1(4)	-0.115(18)						
A_{2g}^4	70.1(1.7)	4.7(4)	-0.103(16)						
E_g^8	73.2(1.2)	4.75(26)	-0.106(12)	73.1(4)	4.39(18)	-0.102(14)			
A_{1g}^4	75.8(1.7)	5.0(3)	-0.107(16)	76.4(1.2)	4.89(27)	-0.088(12)			
A_{2g}^5	74.45(28)	6.44(6)	-0.101(27)						
E_g^9	78.3(2.0)	7.1(4)	-0.146(19)						
E_g^{10}	107.5(1.1)	2.33(24)	0.032(11)	110(6)	1.3(1.9)	0.16(0.14)			
A_{1g}^5	107.7(8)	3.57(18)	-0.024(8)	107(1)	2.62(22)	0.011(10)			
E_g^{11}	135.48(20)	1.30(4)	0.0528(19)						
A_{2g}^6	147.70(29)	-0.49(6)	0.0807(28)						

Table S8. Theoretical wavenumbers and pressure coefficients of the IR-active modes (A_{2u}, E_u) and u-type silent modes (A_{1u}) of the P-3c1 phase. The colors correspond to those in the legend of **Figure S9**.

	Fits $\omega_0 + aP + bP^2$		
Assignment	**Calculations**		
	ω_0 (cm^{-1})	a (cm^{-1}/GPa)	b (cm^{-1}/GPa^2)
E_u^1	25.6(4)	5.18(9)	-0.132(4)
A_{2u}^1	25.5(9)	7.46(20)	-0.282(9)
E_u^2	35.3(1.5)	5.0(3)	-0.130(14)
A_{1u}^1	35.1(1.1)	4.36(24)	-0.094(11)
E_u^3	39.8(1.1)	4.74(24)	-0.113(11)
E_u^4	42.5(1.3)	4.71(28)	-0.110(12)
A_{2u}^2	48.9(2.9)	3.8(6)	-0.083(28)
E_u^5	55.6(3.6)	6.1(8)	-0.21(3)
A_{1u}^2	54.6(1.8)	4.6(4)	-0.115(18)
E_u^6	62.9(2.4)	5.0(5)	-0.115(23)
A_{2u}^3	60.2(1.5)	5.8(3)	-0.160(15)
A_{1u}^3	61.9(1.2)	4.64(26)	-0.112(12)
A_{2u}^4	71(4)	6.5(8)	-0.17(4)
A_{1u}^4	75(4)	6.4(8)	-0.18(4)
E_u^7	71.1(1.9)	5.4(4)	-0.147(18)
E_u^8	74.7(2.6)	5.9(6)	-0.170(25)
A_{1u}^5	76.7(1.4)	7.03(29)	-0.133(13)
A_{2u}^5	76.5(1.0)	6.58(22)	-0.116(10)
E_u^9	80.1(2.3)	5.6(5)	-0.080(22)
E_u^{10}	80.3(1.3)	7.72(28)	-0.171(13)
E_u^{11}	107.9(1.0)	3.65(22)	-0.03(1)
A_{1u}^6	107.3(1.4)	3.6(3)	-0.005(14)
A_{2u}^6	131.3(1.6)	0.0(3)	0.097(15)
E_u^{12}	134.6(9)	0.34(20)	0.087(9)

4.3. *Pm*-3*n* phase

According to group theory,[35] the *Pm*-3*n* phase (S.G. No. 223) of CsI_3 (with two atoms at the *2a and 6c* Wyckoff sites) has 24 vibrational modes (21 optical and 3 acoustic). The mechanical representation at the Brillouin zone center (Γ point) is as follows:

Γ_{24}: $A_{2g}(s) + E_g(R) + T_{2g}(R) + 2T_{1u}(IR) + T_{1g}(S) + 2T_{2u}(S) + T_{1u}(ac)$

where R and IR stand for Raman- and infrared-active, respectively; S stands for silent; and ac stands for acoustic.

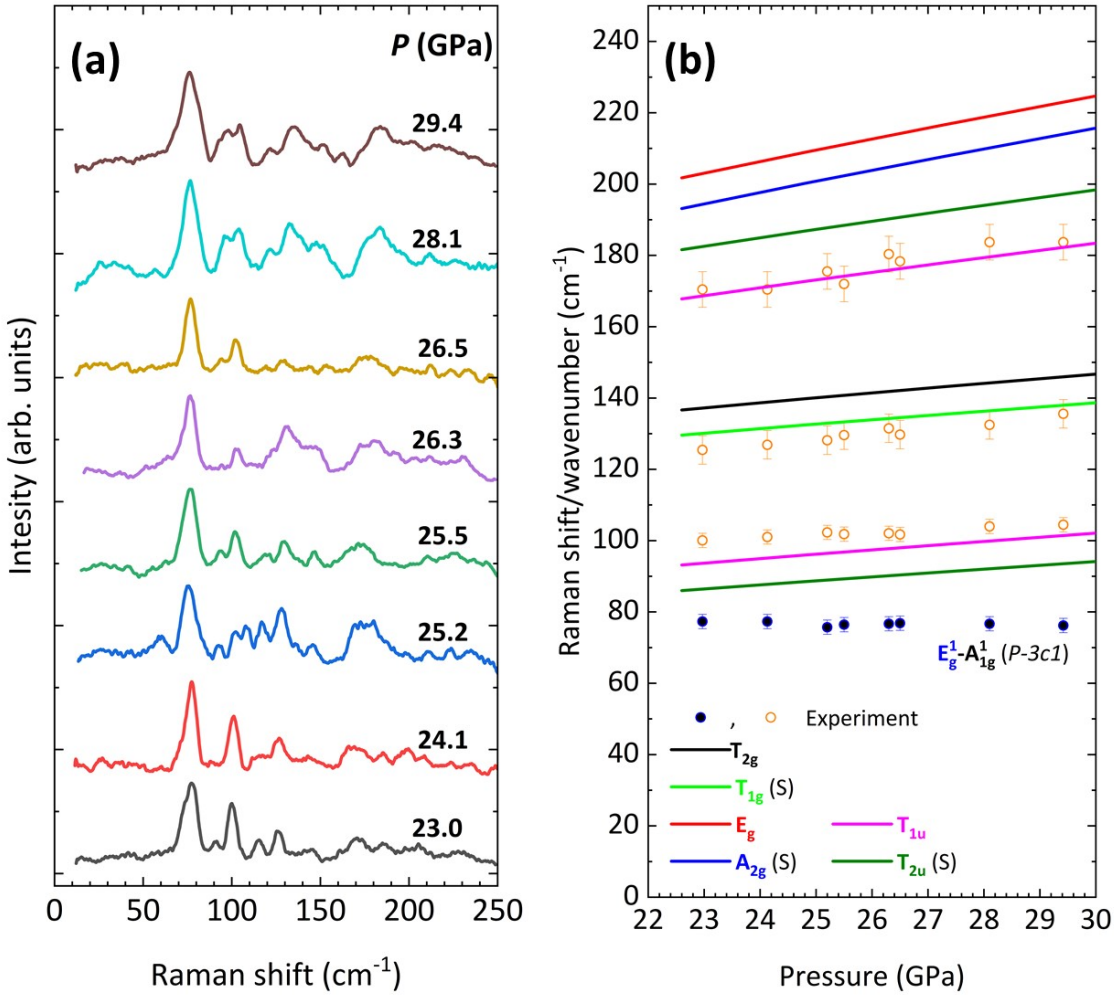

Figure S10. *Pm*-3*n* phase. (a) Selection of Raman spectra at different pressures. (b) Pressure dependence of the experimental (symbols) and theoretical (lines) Raman mode wavenumbers. Theoretical IR-active and silent modes have been added for comparison with the experimentally found Raman bands. Owing to the experimental broadening, the error bars for the modes of this phase have been added, corresponding to half of the width of the Voigt profile as reported by the *Fityk* program.[2]

Table S9. Experimental and theoretical wavenumbers and pressure coefficients of the vibrational Raman and IR modes of the *Pm*-3n phase (linear fit), with tentative symmetry assignment of experimentally measured Raman bands. Silent modes are indicated by (S). Note that in this table, ω_0 refers to the value at 22.6 GPa. The weakly softening phonon at 77.1 cm^{-1} is likely a remnant, corresponding to a second-order mode combination (subtraction) of the coalescing E_g^1 and A_{1g}^1 modes of the *P*-3*c*1 phase, as indicated in the last row (below the dashed line). The colors in the assignment correspond to those in the legend of **Figure S10b**.

Assignment (Raman)		**Fits** $\omega_0 + aP$ Calculations		**Assignment** (IR)		**Fits** $\omega_0 + aP$ Calculations		**Fits** $\omega_0 + aP$ Experiment	
		ω_0 (cm^{-1})	a (cm^{-1}/GPa)			ω_0 (cm^{-1})	a cm^{-1}/GPa	ω_0 (cm^{-1})	a (cm^{-1}/GPa)
T_{1g}	(S)	129.8(6)	1.155(22)	T_{2u}^1	(S)	86.1(4)	1.058(14)	99.2(2)	0.66(8)
T_{2g}		136.9(7)	1.287(23)	T_{1u}^1		93.4(6)	1.145(20)	125(3)	1.53(14)
A_{2g}	(S)	193.7(1.4)	2.90(5)	T_{1u}^2		168.2(1.0)	2.01(3)	168(11)	2.4(4)
E_g		202.3(1.5)	2.95(5)	T_{2u}^2	(S)	182.0(1.0)	2.16(4)		
E_g^1-A_{2g}^1 (*P*-3*c*1)								77.1(2)	-0.1(1)

4.4. Discussion of the three stages of the process of multicenter bond formation from the vibrational point of view

We have mentioned previously that a recently proposed theory of multicenter bonding establishes that the process of formation of multicenter bonds from original primary and secondary (or *incipient*) bonds is a three-stages process.[27,28] Each one of these stages is correlated with a different behavior of the high-wavenumber vibrational modes with increasing pressure. In stage 1, both primary and secondary bond lengths exhibit a decrease at HP. Usually primary bonds are iono-covalent bonds and secondary bonds are non-covalent interactions; e.g. Van der Waals interactions. Consequently, the high-wavenumber vibrational modes (related to stretching vibrations) show positive pressure coefficients. In stage 2, the primary bonds exhibit an anomalous increase of their length at HP, leading to negative pressure coefficients for their associated high-wavenumber vibrational modes (*soft behavior*). Finally, in stage 3, multicenter bonds (either EDMBs or ERMBs) are completely formed and they contract with pressure, as usual atomic bonds. Their associated high-wavenumber vibrational modes acquire again positive pressure coefficients, similarly as the typical iono-covalent bonds in stage 1.

With regard to CsI_3, the occurrence of the aforementioned three stages has already commented in section 3.3 from the structural point of view. On the other hand, an accurate analysis of the vibrational features of CsI_3 under compression independently confirms the mechanism detailed above. Referring to **Figures S6b and S7,** it is evident how in the *Pnma* phase of CsI_3 high-wavenumber modes have positive pressure coefficients (situated typically above 100 cm^{-1}), as expected from stage 3 dominated by ERMBs. Similarly, for the *Pm*-3*n* phase all the vibrational modes show ordinary positive pressure coefficients, as expected for stage 3 (see **Figure S10b**), once EDMBs are formed (all multicenter bonds tend to compress at HP irrespective of they being ERMBs or EDMBs). Experimentally, only a single low-wavenumber mode, likely a second-order difference mode E_g^1-A_{2g}^1 (a remnant of the *P*-3*c*1 phase) shows a weakly soft behavior in the *Pm*-3*n* phase (see **Table S9**).

The vibration analysis of the *P*-3*c*1 phase is trickier. In this structure, all high-wavenumber modes (also above 100 cm^{-1}), except the A_{2u} IR mode, apparently exhibit a positive pressure coefficient in the whole range of pressures, from 0 to 20 GPa (see **Figures S8 and S9**). This is at odds with the negative pressure coefficient expected for high-wavenumber modes in stage 2, prior to the formation of EDMBs above 20 GPa. However, a closer inspection of the vibrational modes of this phase confirms that many low-wavenumber vibrational modes (with large pressure coefficients at RP) reduce their pressure coefficients above 4-5 GPa showing, in some cases, a negligible or even a negative slope above certain pressure. These changes can be explained by a concatenation of anticrossings of vibrational modes with the same symmetry that occurs due to the negative pressure coefficients of the high-wavenumber modes in this phase. These anticrossings originate the change of pressure coefficients observed above 4 GPa in Ref. [19].

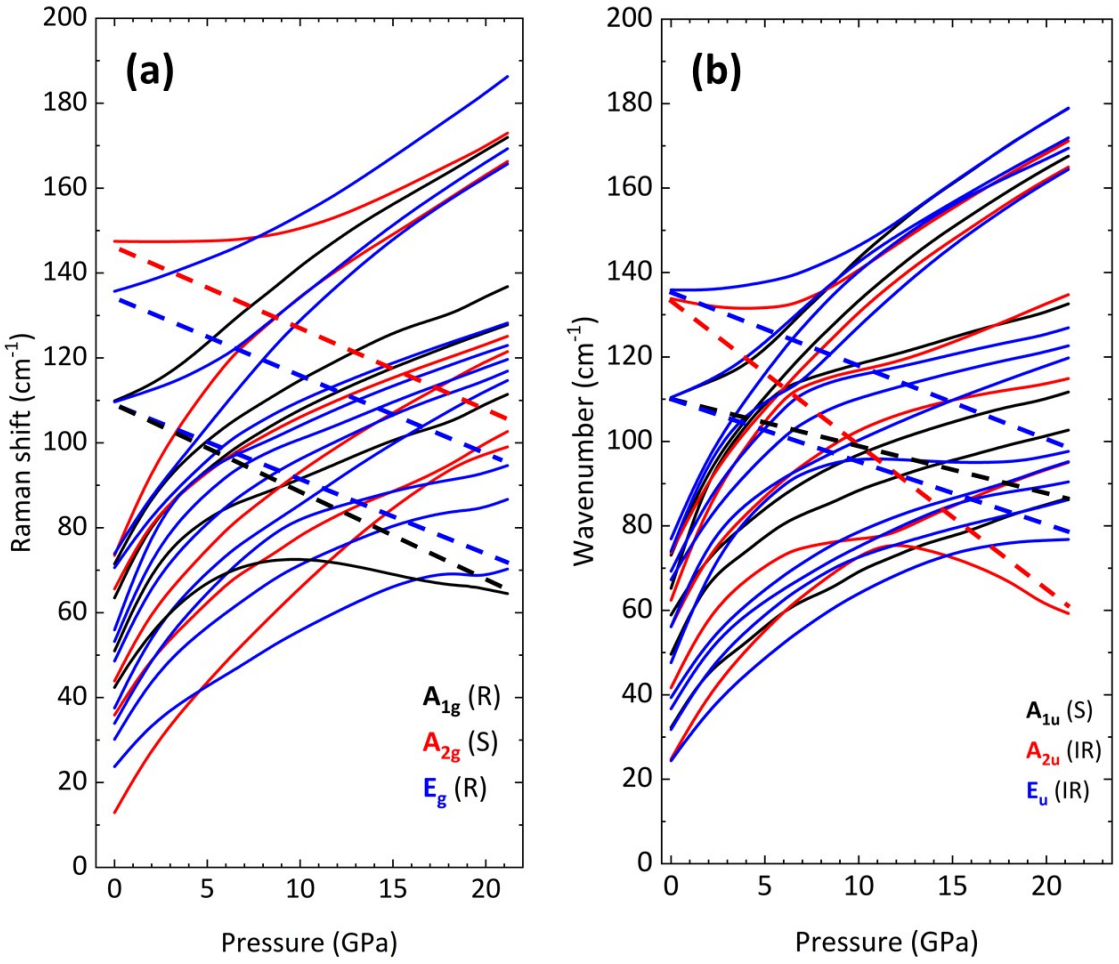

Figure S11. Calculated pressure dependence of the Raman-active (a) and IR-active wavenumbers (b) in the *P*-3*c*1 phase of CsI_3. The soft behavior of some of the high-wavenumber modes in this phase is indicated by bold dashed lines, which show the approximate pressure coefficient of the modes in the absence of anticrossings ("bare" modes).

At first sight, the negative pressure dependence of the high-wavenumber vibrational modes in the *P*-3*c*1 phase is not evident, except for the A_{2u} IR mode, even when we plot the theoretically predicted vibrational modes (**Figure S1110**). To make it clearer, we have shown as colored dashed lines in **Figures S1110a and S1110b** the approximate pressure dependence that these modes would have close to RP in the absence of anticrossing ("bare" modes). The negative dependence on pressure is more easily observed near RP in the modes between 130 and 150 cm^{-1} than in the modes close to 100 cm^{-1}, especially for the A_{2u} mode. The reason behind this is that, in terms of wavenumbers, the large gap existing at RP between the modes with the highest wavenumbers and the topmost low-wavenumber modes (near 80 cm^{-1}) prevents the occurrence of these anticrossings at low pressure. On the contrary, the effect of the anticrossing at RP is much more noticeable for the high-wavenumber modes around 110 cm^{-1} (along with a less noticeable negative pressure coefficient), because there is a much smaller gap between them and the corresponding uppermost low-wavenumber modes.

In summary, the negative pressure coefficients of the "bare" high-wavenumber vibrational modes in the *P*-3*c*1 phase (together with the existence of corresponding

anticrossings), explain the negative pressure coefficients found in low-wavenumber modes at HP.[19] In addition, the negative pressure coefficients of these "bare" modes suggest that the *P*-3*c*1 phase corresponds to stage 2 of the formation of EDMBs (or, at least, to stage 1 up to 6 GPa and to stage 2 above 6 GPa), as commented previously with reference to the experimental bond lengths in Section 3.2 in SI.[20] These results are in full agreement with the recent unified theory of multicenter bonding.[27,28] The only change in CsI_3 with respect to the recent unified theory of multicenter bonding is that EDMBs in the *Pm*-3*n* phase do not come from a primary iono-covalent and a secondary non-covalent interaction but come from a primary ERMB (that present in I_3^- units) and a secondary non-covalent interaction (that present between neighbor I_3^- units) present in the *P*-3*c*1 phase.

5. Analysis of the electron density topology

Table S10. Number of electrons shared (ES) and normalized number of electrons transferred (ET) between two atoms for the short (s) and long (l) I–I bonds in the *P*-3*c*1 phase and for the only I–I bond in the *Pm-3n* phase at selected pressures. Note that in the *P*-3*c*1 phase, the short and long bonds correspond to intramolecular (within I_3^- units) and intermolecular (between I_3^- units) bonds, respectively. The ET values of all I–I bonds are calculated as the difference in Bader charges between neighboring I atoms as provided in **Table S11**.

***P*-3*c*1**					***Pm*-3*n***		
Pressure (GPa)	**ES (s)**	**ET(s)**	**ES (l)**	**ET(l)**	**Pressure** (GPa)	**ES**	**ET**
0.3	1.65	0.32	0.05	0	0.7	0.75	0
16.0	1.34	0.20	0.67	0	16.6	0.64	0
22.6	1.24	0.14	0.93	0	23.5	0.61	0
31.8	1.13	0.06	1.09	0	32.6	0.57	0

Table S11. Bader charges of the independent Cs and I atoms in the *P*-3*c*1, and *Pm*-3*n* phases at selected pressures; $I_{(1)}$ and $I_{(2)}$ indicate the central and terminal I atom in the I_3^- units of the *P*-3*c*1 phase, respectively.

P-3c1				***Pm-3n***		
Pressure (GPa)	q_{Bader}			**Pressure** (GPa)	q_{Bader}	
	Cs	**$I_{(1)}$**	**$I_{(2)}$**		**Cs**	**I**
0.3	0.80	-0.06	-0.38	0.7	0.75	-0.25
16.0	0.67	-0.09	-0.29	16.6	0.64	-0.21
22.6	0.64	-0.12	-0.26	23.5	0.61	-0.20
31.8	0.61	-0.16	-0.22	32.6	0.57	-0.19

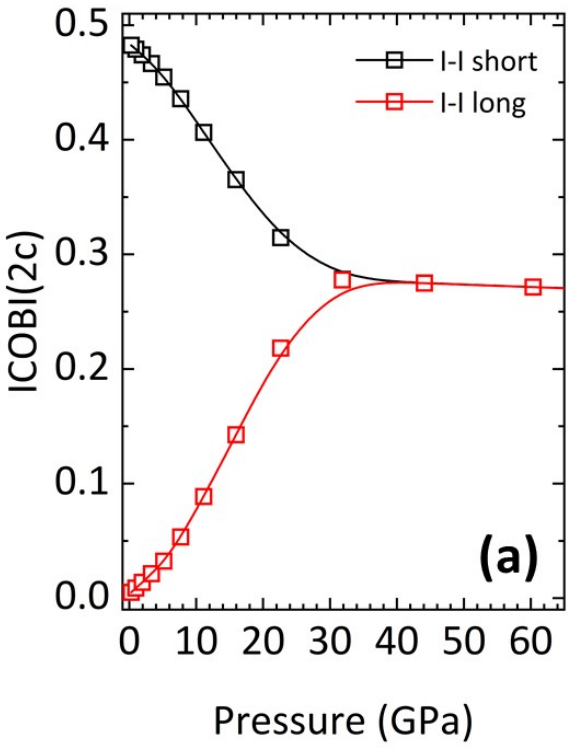

Figure S12. Calculated pressure dependence of the ICOBI(2c) for the short and long I–I bonds in the *P*-3*c*1 phase.

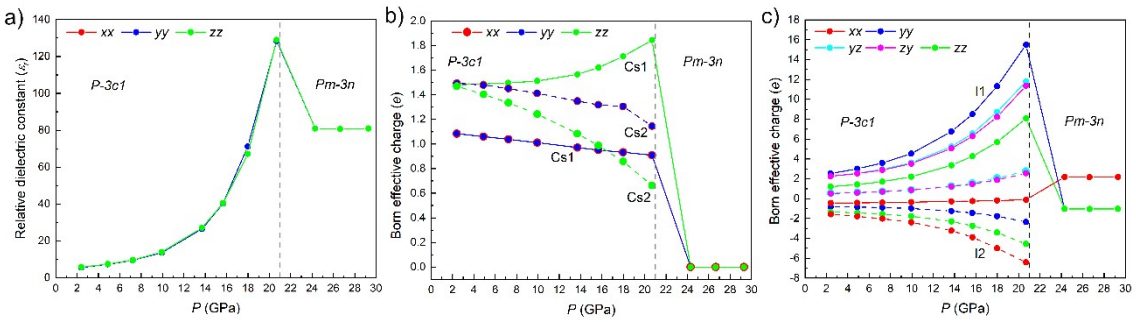

Figure S13. (a) Calculated pressure dependence of the diagonal elements of the optical dielectric constant, ε_∞, matrix in hexagonal (*P*-3*c*1) CsI_3. The calculated pressure dependence of the Born effective charges of Cs (b) and I (c) atoms in the *P*-3*c*1 and *Pm*-3*n* phases of CsI_3.

6. Bibliography

[1] H. K. Mao, J. Xu, P. M. Bell, *Journal of Geophysical Research* 1986, *91*, 4673.
[2] M. Wojdyr, *J Appl Crystallogr* 2010, *43*, 1126–1128.
[3] P. Hohenberg, W. Kohn, *Physical Review* 1964, *136*, B864–B871.
[4] G. Kresse, J. Furthmüller, *Computational Materials Science* 1996, *6*, 15–50.
[5] G. Kresse, J. Furthmüller, *Physical Review B - Condensed Matter and Materials Physics* 1996, *54*, 11169–11186.
[6] P. E. Blöchl, *Physical Review B* 1994, *50*, 17953–17979.
[7] D. Joubert, G. Kresse, D. Joubert, *Physical Review B* 1999, *59*, 1758–1775.
[8] J. P. Perdew, K. Burke, M. Ernzerhof, *Physical Review Letters* 1996, *77*, 3865–3868.
[9] S. Grimme, S. Ehrlich, L. Goerigk, *J Comput Chem* 2011, *32*, 1456–1465.
[10] H. J. Monkhorst, J. D. Pack, *Physical Review B* 1976, *13*, 5188–5192.
[11] K. Parlinski, Z. Q. Li, Y. Kawazoe, *Physical Review Letters* 1997, *78*, 4063–4066.
[12] P. Giannozzi, O. Andreussi, T. Brumme, O. Bunau, M. Buongiorno Nardelli, M. Calandra, R. Car, C. Cavazzoni, D. Ceresoli, M. Cococcioni, N. Colonna, I. Carnimeo, A. Dal Corso, S. De Gironcoli, P. Delugas, R. A. DiStasio, A. Ferretti, A. Floris, G. Fratesi, G. Fugallo, R. Gebauer, U. Gerstmann, F. Giustino, T. Gorni, J. Jia, M. Kawamura, H.-Y. Ko, A. Kokalj, E. Küçükbenli, M. Lazzeri, M. Marsili, N. Marzari, F. Mauri, N. L. Nguyen, H.-V. Nguyen, A. Otero-de-la-Roza, L. Paulatto, S. Poncé, D. Rocca, R. Sabatini, B. Santra, M. Schlipf, A. P. Seitsonen, A. Smogunov, I. Timrov, T. Thonhauser, P. Umari, N. Vast, X. Wu, S. Baroni, *J. Phys.: Condens. Matter* 2017, *29*, 465901.
[13] A. A. Mostofi, J. R. Yates, Y.-S. Lee, I. Souza, D. Vanderbilt, N. Marzari, *Computer Physics Communications* 2008, *178*, 685–699.
[14] A. Otero-de-la-Roza, E. R. Johnson, V. Luaña, *Computer Physics Communications* 2014, *185*, 1007–1018.
[15] A. Dal Corso, *Computational Materials Science* 2014, *95*, 337–350.
[16] A. Otero-de-la-Roza, Á. Martín Pendás, E. R. Johnson, *J. Chem. Theory Comput.* 2018, *14*, 4699–4710.
[17] P. C. Müller, C. Ertural, J. Hempelmann, R. Dronskowski, *J. Phys. Chem. C* 2021, *125*, 7959–7970.
[18] R. Nelson, C. Ertural, J. George, V. L. Deringer, G. Hautier, R. Dronskowski, *J Comput Chem* 2020, *41*, 1931–1940.
[19] N. N. Patel, M. Sunder, A. B. Garg, H. K. Poswal, *Phys. Rev. B* 2017, *96*, 174114.
[20] T. Poręba, S. Racioppi, G. Garbarino, W. Morgenroth, M. Mezouar, *Inorg. Chem.* 2022, *61*, 10977–10985.
[21] P. Vinet, J. R. Smith, J. Ferrante, J. H. Rose, *Phys. Rev. B* 1987, *35*, 1945–1953.
[22] F. Birch, *Journal of Geophysical Research* 1952, *57*, 227–286.
[23] M. Savastano, *Dalton Trans.* 2021, *50*, 1142–1165.
[24] R. C. L. M. Slater, *Acta Cryst* 1959, *12*, 187–196.
[25] J. C. Slater, *Acta Cryst* 1959, *12*, 197–200.
[26] F. J. Manjón, H. H. Osman, M. Savastano, Á. Vegas, *Materials* 2024, *17*, 2840.
[27] H. H. Osman, A. Otero-de-la-Roza, P. Rodríguez-Hernández, A. Muñoz, F. J. Manjón, *J. Mater. Chem. C* 2024, *12*, 10447–10474.
[28] H. H. Osman, P. Rodríguez-Hernández, A. Muñoz, F. J. Manjón, *J. Mater. Chem. C* 2025, *13*, 3774–3803.
[29] K. Cao, X.-X. Qu, H. Jiang, Y.-H. Su, C. Zhang, G. Frapper, *J. Phys. Chem. C* 2019, *123*, 30187–30197.

[30] Y. Fu, F. Li, X. Zhang, C. Wang, X. Liu, G. Yang, *Journal of Alloys and Compounds* 2022, *923*, 166465.
[31] M. Savastano, H. H. Osman, Á. Vegas, F. J. Manjón, *Chem. Commun.* 2024, *60*, 12677–12689.
[32] T. Poręba, M. Świątkowski, R. Kruszyński, *Dalton Trans.* 2021, *50*, 2800–2806.
[33] S. Madhu, H. A. Evans, V. V. T. Doan-Nguyen, J. G. Labram, G. Wu, M. L. Chabinyc, R. Seshadri, F. Wudl, *Angew Chem Int Ed* 2016, *55*, 8032–8035.
[34] D. Wang, H. Zhang, W. W. Yu, Z. Tang, *J. Phys. Chem. Lett.* 2017, *8*, 2463–2468.
[35] E. Kroumova, M. L. Aroyo, J. M. Perez-Mato, A. Kirov, C. Capillas, S. Ivantchev, H. Wondratschek, *Phase Transitions* 2003, *76*, 155–170.
[36] P. Deplano, J. R. Ferraro, M. L. Mercuri, E. F. Trogu, *Coordination Chemistry Reviews* 1999, *188*, 71–95.